Degradation of the internal tide over long bumpy topography

Erinna Chen

1 Introduction

Internal waves in the ocean carry a significant amount of energy and are the main cause of diapycnal mixing in the ocean. Barotropic tidal currents flowing over topography generate a large number of these internal waves, also known as internal tides. From TOPEX/Poseidon altimetry data, it is estimated that up to 1 TW of power is transferred away from the barotropic tides in the deep ocean, primarily by internal tides [7].

The generation of the internal tides over topography has been extensively studied (e.g. [5], [2], [9], [3]) and it is suggested that in an ocean of finite-depth, the primary waves generated are those of low baroclinic modes [17]. However, mechanisms for internal-tide-driven mixing and energy dissipation such as shear instability, wave-wave interactions and parametric subharmonic instability are most effective at high (i.e. greater than wavenumber 10) modes. The transition from the low-mode internal tides to higher mode waves where mixing can occur is poorly understood. It is important to understand where these processes occur in that different parameterizations of internal wave dissipation may significantly alter the behavior of ocean circulation in models [8].

Low-mode internal tides have been observed to propagate over O(1000 km) distances from their generation site [6], [15]. It is likely that over this distance, the internal tides should encounter varying bottom topography that would scatter the low mode waves into higher modenumbers. Topographic scattering in the deep ocean has been studied extensively in two main contexts: generation of the internal tide and scattering of internal waves over finite-length topography (e.g. [1], [12], [13], [16]). However, little work has looked at internal wave propagation over topography with multiple bumps, random topography, or topography with long extent.

In this work, we study the degradation of the internal tide first by extending methods previously utilized to understand the conversion of the barotropic tide and also by using a ray tracing method. We primarily studied the behavior of the internal tide propagating over well-behaved "model" topographies; however, there are ways to extend this work to include more random topography.

2 Governing equations

We begin by considering the dynamics of an incompressible, hydrostatic, stratified fluid governed by the linear Boussinesq equations in two-dimensions (x and z):

$$u_t + P_x = 0, \tag{1}$$
$$w_t + P_z = b, \tag{2}$$
$$b_t + N^2 w = 0, \tag{3}$$
$$u_x + w_z = 0, \tag{4}$$

where N is the buoyancy frequency defined as

$$N^2 = -g\frac{d\ln\bar{\rho}_0}{dz}.$$

We will only consider constant bouyancy frequency. We employ subscript notation throughout to represent partial differentiation.

The momentum equations can be combined by differentiating (1) with respect to z, (2) with respect to x, and then adding, resulting in a vorticity equation:

$$(u_z - w_x)_t + b_x = 0. \tag{5}$$

By expressing the velocities u and w in terms of a streamfunction ψ where

$$u = \psi_z,\ w = -\psi_x, \tag{6}$$

the vorticity and buoyancy equations ((5), (3), respectively) can be combined into a single wave equation:

$$\left(\nabla^2\psi\right)_{tt} + N^2\psi_{xx} = 0 \tag{7}$$

2.1 Stable solutions to the wave equation

We now seek stable solutions to equation (7) of the form

$$\psi = \hat{\psi}(x,z)e^{-i\omega t}. \tag{8}$$

By substituting (8) into the wave equation (7), the streamfunction now satisfies

$$\hat{\psi_{zz}} = \left(\frac{N^2}{\omega^2} - 1\right)\hat{\psi_{xx}}. \tag{9}$$

This equation can be scaled and non-dimensionalized via the transform

$$x \to \frac{H}{\pi}\sqrt{\frac{N^2-\omega^2}{\omega^2}}x',\ z \to \frac{H}{\pi}z',$$

resulting in a scaled, non-dimensional form for the wave equation

$$\hat{\psi_{x'x'}} = \hat{\psi_{z'z'}}. \tag{10}$$

From this point forth, we will only be considering waves in their scaled, non-dimensional form and therefore, we drop the "prime" and "hat" notation.

While we have neglected to include the effects of rotation in deriving (10), rotation can easily be included and only appears in the scaling. The scaling is such that the wave crests propagate at 45°.

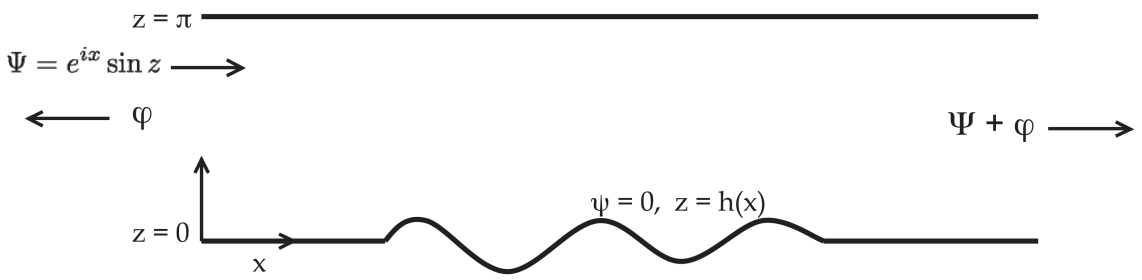

Figure 1: Schematic of problem setup. The ocean has finite depth, and in scaled coordinates z extends from 0 to π. The radiation conditions require that the scattered wave component φ propagate outwards. The internal tide Ψ is a mode-1 wave that enters from the left of the topography and propagates rightward over the topography. The topography is given as $z = h(x)$ where $h(x) = 0$ in the left and right far-fields.

3 Scattering of the internal tide over weak topography

The scattering of internal waves over topography has been studied extensively in the context of barotropic tidal conversion (e.g. [5], [9], [3], [10]). While some of these previous calculations can account for topography that is steep (i.e. slopes greater than 1) or has finite to large-amplitude, the most analytically tractable problem involves topography in the so-called "weak topography" limit. For the weak topography limit to be appropriate, the amplitude of the topography must be much small than the vertical scales of the waves and the topographic slopes are much less than the slope of a tidal beam ($s = 1$ in our reference frame). If this is the case, the boundary condition can be applied at the flat surface, instead of on the topography. We adopt a method of analysis similar to [5], but extend this for the internal tide propagating over weak topography. One notable difference in our setup is that while typically the barotropic tide is assumed to be an infinite source of energy, the internal tide has finite energy and will degrade as it propagates.

We begin by approximating the internal tide as a single, mode-1 wave given by

$$\Psi = e^{ix} \sin z. \tag{11}$$

The internal tide has finite amplitude (and energy), and our goal is to understand how this amplitude decays as a function of the bottom topography. Figure 1 is a schematic of the problem. The internal tide is assumed to propagate from left to right in the domain. The topography is given by $h(x)$, where $h(x) = 0$ in the far-fields (both right and left).

Throughout the domain, the streamfunction ψ can be expressed as

$$\psi = \Psi + \varphi, \tag{12}$$

where Ψ represents the internal tide and φ represents the scattered waves due to interaction with the topography. The scattered waves are subject to radiation conditions in the far-field, that is, on the left and right boundaries of the domain, the scattered waves must propagate

outwards. In addition, the streamfunction ψ is subject to the boundary conditions

$$\psi = 0 \text{ at } z = h(x), \tag{13}$$

$$\psi = 0 \text{ at } z = \pi. \tag{14}$$

Thus, this requires that along the bottom boundary

$$\varphi = -\Psi = -e^{ix}\sin(h(x)) \text{ at } z = h(x). \tag{15}$$

For weak topography, we can expand this boundary condition around $z = 0$, resulting in the $O(1)$ boundary condition

$$\varphi = -e^{ix}h(x) \text{ at } z = 0. \tag{16}$$

In order to understand how the mode-1 internal tide is scattered to higher modenumbers, we express the scattered wave component of the streamfunction as a Fourier series,

$$\varphi = \sum_{n=1}^{\infty} \varphi_n \sin nz. \tag{17}$$

The scattering coefficients φ_n can be obtained first by carrying out a Galerkin projection of φ_{zz} onto $\sin nz$.

$$\int_0^{\pi} \varphi_{zz} \sin nz \; dz = -nhe^{ix} - \frac{n^2\pi}{2}\varphi_n. \tag{18}$$

By integrating the left hand side of equation (18) and substituting for φ_{zz} using the wave equation (10), we obtain

$$\frac{d^2\varphi_n}{dx^2} + n^2\varphi_n = \frac{-2}{\pi}nhe^{ix}. \tag{19}$$

This differential equation can be solved using a Green's function

$$\frac{d^2 g_n}{dx^2} + n^2 g_n = \delta(x). \tag{20}$$

subject to the radiation conditions. Thus, g_n is given by

$$g_n = \frac{1}{2in}^{\,in|x|} \tag{21}$$

and the scattering coefficients φ_n are

$$\varphi_n(x) = \frac{-2n}{\pi}\int_{-\infty}^{\infty} g_n(x-x')h(x')e^{ix'}dx' = \frac{i}{\pi}\int_{-\infty}^{\infty} e^{in|x-x'|+ix'}h(x')dx'. \tag{22}$$

While equation (22) gives us information about the scattered wavefield over the entire domain, we are particularly interested in the scattered waves that propagate away from the topography. In the far fields, the scattered waves must satisfy the radiation conditions

$$\text{(left) } x \to -\infty : \varphi \to \sum_{n=1}^{\infty} a_n e^{-inx}\sin nz, \tag{23}$$

$$\text{(right) } x \to +\infty : \varphi \to \sum_{n=1}^{\infty} b_n e^{inx}\sin nz. \tag{24}$$

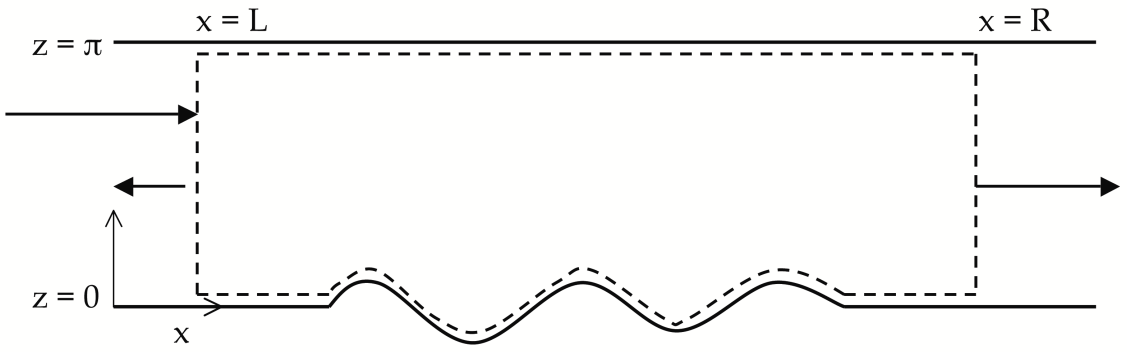

Figure 2: Energy flux is constant through the domain indicated by the dashed region. A finite amount of energy enters the domain via the internal tide on the left side of the topography and leaves the domain via waves in both directions.

By combining (22)-(24), we obtain the scattering coefficients in the far-fields

$$\text{(left) } x \to -\infty : \varphi_{Ln} = \frac{i}{\pi} \int_{-\infty}^{\infty} e^{i(n+1)x'} h(x') dx', \tag{25}$$

$$\text{(right) } x \to +\infty : \varphi_{Rn} = \frac{i}{\pi} \int_{-\infty}^{\infty} e^{-i(n-1)x'} h(x') dx'. \tag{26}$$

This solution is known in other contexts as Bragg scattering. Knowing the scattering coefficients now allows us to calculate the amount of energy converted from the internal tide to higher mode numbers.

3.1 Scattered wave energy flux

The full streamfunction ψ satisfies

$$\overrightarrow{\nabla} \cdot \overrightarrow{\mathcal{J}} = 0, \tag{27}$$

where $\mathcal{J}$ represents the flux and is defined as

$$\overrightarrow{\mathcal{J}} = i \left[(\psi \psi_x^* - \psi^* \psi_x), -(\psi \psi_z^* - \psi^* \psi_z) \right]. \tag{28}$$

Integrating over the domain $x = [L, R]$ and $z = [0, \pi]$ as illustrated in figure 2, we find that

$$\int_0^\pi (\psi \psi_x^* - \psi^* \psi_x)\, dz \Big|_{x=R} - \int_0^\pi (\psi \psi_x^* - \psi^* \psi_x)\, dz \Big|_{x=L} = 0, \tag{29}$$

that is the horizontal energy flux through the domain is zero.

If we now substitute $\psi = \Psi + \varphi_L$ at $x = L$ and $\psi = \Psi + \varphi_R$ at $x = R$ into equation (29), we find that the energy loss from the internal tide is a function of the scattered wave coefficients,

$$\Delta E_{IT} = -\frac{1}{2} \sum_{n=1}^{\infty} n \left(|\varphi_{Rn}|^2 + |\varphi_{Ln}|^2 \right). \tag{30}$$

3.2 Scattered wave solutions for model topographies

For the topographies

$$h(x) = \frac{1}{2}\epsilon \cos kx$$
$$h(x) = \frac{1}{2}\epsilon(\cos kx + 1),$$

the integrals for the scattering coefficients (25, 26) can be evaluated analytically. Assuming the topography is located only on the interval $[-b\pi, b\pi]$, vanishes at $x = -b\pi$ and $x = b\pi$, and is zero elsewhere, then the scattering coefficients are

$$\varphi_{Ln} = \frac{i\epsilon}{4\pi} \int_{-b\pi}^{b\pi} e^{i(n+1)x'} \left(e^{ikx'} + e^{-ikx'} + 2\alpha \right) dx' \tag{31}$$

$$\varphi_{Rn} = \frac{i\epsilon}{4\pi} \int_{-b\pi}^{b\pi} e^{-i(n-1)x'} \left(e^{ikx'} + e^{-ikx'} + 2\alpha \right) dx' \tag{32}$$

where $\alpha = 0$ or 1.

For the model topographies, this solution suggests that there are a limited number of scattered waves. To the right of the topography, the scattered waves occur as a $n = 1$ mode and a $n = k + 1$ mode. To the left of the topography, there is a single scattered wave, the $n = k - 1$ mode. The amplitudes of these waves depend on the length of the topography, b, and the height of the topography, ϵ,

$$\begin{aligned} |\varphi_{R1}| &= \alpha\epsilon b \\ |\varphi_{R,k+1}| &= \frac{1}{2}\epsilon b \\ |\varphi_{L,k-1}| &= \frac{1}{2}\epsilon b. \end{aligned} \tag{33}$$

From (30), the energy drained from the internal tide is the sum of the product of the wavenumbers and their corresponding wave amplitude,

$$\Delta E_{IT} = -\frac{1}{2}\left(\alpha\epsilon b + \frac{1}{2}(k+1)\epsilon b + \frac{1}{2}(k-1)\epsilon b \right). \tag{34}$$

However, the amount of energy drained from the internal tide is not finite in this solution. For fixed ϵ, the drained energy grows unbounded with the length of the topography, b.

4 Scattered wave solutions using a Green's function approach

Equation (34) suggests that our solution for the scattered wave coefficients has a limited range of validity. This may be due to an inconsistency in the boundary condition expansion. To $O(\epsilon)$ the bottom boundary condition is

$$-\epsilon h e^{ix} = \varphi(x, 0) + \epsilon h \varphi_z(x, 0). \tag{35}$$

Previously, the solution in §3 did not include the second term on the right hand side.

To rectify this problem, we now incorporate the fully non-linear bottom boundary condition (15) by utilizing a method previously used in calculations of wave scattering off finite and supercritical topography (e.g. [3], [14]). We define a Green's function as

$$G(x-x',z,z') = \frac{1}{\pi}\sum_{n=1}^{\infty}\frac{1}{n}e^{in|x-x'|}\sin nz\sin nz' \tag{36}$$

The scattered component of the streamfunction is given by

$$\varphi = \int_{-a}^{a}\gamma(x')G(x-x',z,h(x'))dx' \tag{37}$$

where the topography lies between $[-a,a]$ and $\gamma(x)$ is the source density function representing the topography. $\gamma(x)$ is found through the solution of a matrix problem incorporating the bottom boundary condition

$$-e^{ix}\sin h(x) = \int_{-a}^{a}\gamma(x')G(x-x',h(x),h(x'))dx'. \tag{38}$$

Once we have the source density function, the full solution for the scattered wave field is given by

$$\varphi(x,z) = \int_{-a}^{a}\gamma(x')\sum_{n=1}^{\infty}\frac{1}{\pi n}e^{in|x-x'|}\sin nz\sin nh(x')dx' \tag{39}$$

The scattered wave field to the left of the topography is

$$\varphi_L(x,z) = \sum_{n=1}^{\infty}e^{-inx}\sin nz\frac{1}{\pi n}\int_{-a}^{a}\gamma(x')e^{inx'}\sin nh(x')dx'. \tag{40}$$

The corresponding modal scattering coefficients are thus

$$\varphi_{Ln}(x) = e^{-inx}\frac{1}{\pi n}\int_{-a}^{a}\gamma(x')e^{inx'}\sin nh(x')dx'. \tag{41}$$

Similarly, to the right of the topography, the scattered wave field is

$$\varphi_R(x,z) = \sum_{n=1}^{\infty}e^{inx}\sin nz\frac{1}{\pi n}\int_{-a}^{a}\gamma(x')e^{-inx'}\sin nh(x')dx', \tag{42}$$

and the corresponding scattering coefficients are

$$\varphi_{Rn}(x) = e^{inx}\frac{1}{\pi n}\int_{-a}^{a}\gamma(x')e^{-inx'}\sin nh(x')dx'. \tag{43}$$

For this formulation, the scattering coefficients must be solved for numerically. The numerical code we employ takes an input for the topography $h(x)$, solves for the source function $\gamma(x)$ and then solves for the scattering coefficients. The Green's function defined in (36) has the limitation that the topography must lie above the flat bottom ($z = 0$). However, by using the Green's function approach, the topography is not limited to the weak topography regime and thus, may be used to model more "realistic" topography than our model topography.

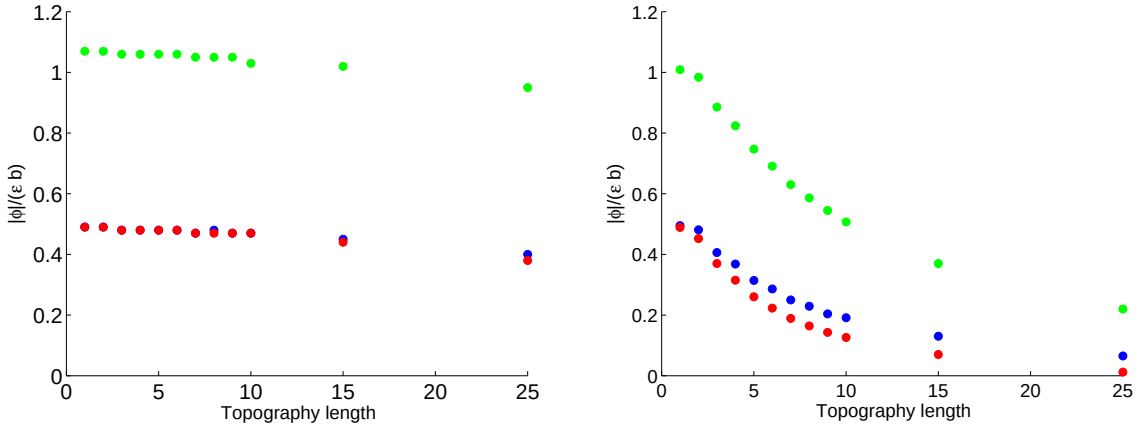

Figure 3: Scattering coefficients solved for using the Green's function method for the predicted modes from (33), φ_{R1}(green), $\varphi_{R,k+1}$(red), $\varphi_{L,k-1}$(blue), shown with $k = 5$. Solution from (33) suggests that $\frac{\varphi_n}{\epsilon b}$ should remain constant, independent of topography length. (a) Coefficients for $\epsilon = 0.01$ (b) Coefficients for $\epsilon = 0.1$

4.1 Numerical solutions for the wave equation

For the model topography $h(x) = \frac{1}{2}(\cos kx + 1)$, the scattered wave solution found in §3.2 says that there are only three scattered waves and that the parameter $\frac{\varphi_n}{\epsilon b}$ should remain constant. As stated before, the range of validity for this solution must be limited because the internal tide has finite energy. Figures 3 and 4 show results of solutions from the Green's function approach for variable length topography.

Figure 3 shows the scattering coefficients for the three predicted modes from (33), i.e. the modes φ_{R1}, $\varphi_{R,k+1}$, and $\varphi_{L,k-1}$. For figure 3a, the topography is extremely weak, ϵ equals 0.01. In this case, the prediction that $\frac{\varphi_n}{\epsilon b}$ remains constant seems to hold even for fairly long topography. However, for topography of higher amplitude (figure 3b), the Green's function solution diverges significantly from the prediction even for short topographic lengths (i.e. 2-3 wavelengths).

Figure 4 shows the full spectrum of the scattering coefficients for topography with $\epsilon = 0.1$. The peaks of the spectrum are the three modes predicted from the linear solution (shown in red); however, there is a significant amount of energy also contained in higher harmonic modes. The harmonic modes are the $nk - 1$ modes on the left of the topography and the $nk + 1$ modes on the right of the topography, where $n = 2, 3, \ldots$. The divergence of the actual solution and the predicted solution in figure 3b is likely due to the presence of these higher-order harmonics. As the topography gets longer, more energy from the internal tide is lost to these harmonics.

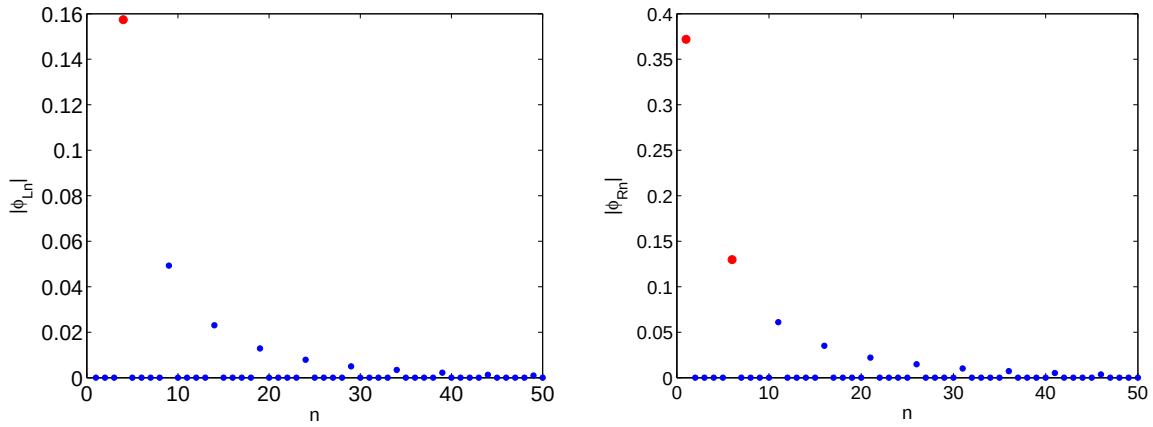

(a) (b)

Figure 4: Scattering coefficients solved for using the Green's function method for $h(x) = \frac{1}{2}(0.1)(\cos 5x + 1)$. Red dots indicate modes predicted from (33). (a) Scattering coefficients to the left of the topography (b) Scattering coefficients to the right of the topography

5 Multiscale asymptotic analysis

While the Green's function method may allow us to incorporate the fully nonlinear bottom boundary condition, but solving for the source function is computationally expensive. The scattered wave solution given in §3.2 suggests that the range of validity for our solution may be extended if we introduce another length scale.

In the classic fashion, we introduce a long horizontal scale

$$X = \epsilon x \tag{44}$$

such that

$$\frac{\partial}{\partial x} \rightarrow \frac{\partial}{\partial x} + \epsilon \frac{\partial}{\partial X}. \tag{45}$$

The streamfunction can be written in expanded form as

$$\psi = \psi^{(0)}(x, z, X) + \epsilon \psi^{(1)}(x, z, X) + O(\epsilon^2) \tag{46}$$

where the superscripts represent the order of the expansion. Plugging (46) into the wave equation, the $O(1)$ equation on ψ is

$$\psi^{(0)}_{xx} - \psi^{(0)}_{zz} = 0. \tag{47}$$

Thus to zeroth order, the streamfunction satisfies the wave equation. In order to solve for $\psi^{(0)}(x, z, X)$, we must expand to next order in ϵ. To $O(\epsilon)$, ψ satisfies

$$\psi^{(1)}_{xx} - \psi^{(1)}_{zz} = -2\psi^{(0)}_{xX}. \tag{48}$$

We prescribe that the solvability condition on ψ is that the $O(1)$ solution is periodic on the fast length scale x. We then expand $\psi^{(0)}$ as a Fourier series of the form

$$\psi^{(0)}(x,z,X) = \sum_{n=1}^{\infty} \left(T_n(X)e^{inx} + R_n(X)e^{-inx}\right) \sin nz \tag{49}$$

where T_n are the transmitted waves (equivalent to φ_{Rn} on the far right) and R_n are the reflected waves (equivalent to φ_{Ln} on the far left). This expansion of $\psi^{(0)}$ satisfies the $O(1)$ boundary condition on the bottom

$$\psi^{(0)}(x,0,X) = 0. \tag{50}$$

Substituting for $\psi^{(0)}$ in (48) gives

$$\psi^{(1)}_{xx} - \psi^{(1)}_{zz} = -2i \sum_{n=1}^{\infty} n \left(T_n(X)e^{inx} + R_n(X)e^{-inx}\right) \sin nz. \tag{51}$$

The coefficients T_n and R_n are a function of the bottom topography and can be solved for by manipulating equation (51) and applying the bottom boundary condition. To solve for T_n, we multiply both sides of (51) by $e^{-inx}\sin nz$ and integrate over the domain. Because of orthogonality and periodicity, the right hand side of the equation reduces to

$$\int_{-\pi}^{\pi}\int_{0}^{\pi} -2i \sum_{m=1}^{\infty} m \left(T_m(X)e^{imx} + R_n(X)e^{-imx}\right) \sin mz \sin nz \; e^{-inx} dz \; dx = -i2\pi^2 n T_{nX}. \tag{52}$$

The left hand side simplifies to

$$\int_0^{\pi}\int_{-\pi}^{\pi} \psi^{(1)}_{xx} - \psi^{(1)}_{zz} dx dz = -\int_{-\pi}^{\pi} n\psi^{(1)}(x,X,0)e^{-inx} dx \tag{53}$$

The $O(\epsilon)$ boundary condition that must be satisfied is

$$\psi^{(1)}(x,0,X) = -h(x)\psi^{(0)}_z(x,0,X). \tag{54}$$

By combining (52)-(54), we obtain the equation for the evolution of the transmitted wave coefficients,

$$T_{nX} = \frac{i}{2\pi^2}\int_{-\pi}^{\pi} h(x)e^{-inx} \sum_{m=1}^{\infty} \left(T_m e^{imx} + R_m e^{-imx}\right) dx. \tag{55}$$

Similarly, the reflected wave coefficients, R_n, can be obtained by multiplying (51) by $e^{inx}\sin nz$ and integrating over the domain. The reflected wave coefficients satisfy

$$R_{nX} = \frac{i}{2\pi^2}\int_{-\pi}^{\pi} h(x)e^{inx} \sum_{m=1}^{\infty} \left(T_m e^{imx} + R_m e^{-imx}\right) dx. \tag{56}$$

Equations (55) and (56) suggest that the long-length scale evolution of the transmitted and reflected waves are coupled to each other by their short-scale behavior over the topography.

5.1 Solutions for model topographies

In the case of our model topographies, the evolution equations (55) and (56) take on a form that is readily solvable.

5.1.1 General solutions for $k > 0$

Substituting our model topography,

$$h(x) = \frac{1}{2}(\cos kx + \alpha) \text{ where } \alpha = 0 \text{ or } 1,$$

into (55) and (56), the transmitted waves and reflected waves are given by

$$T_{nX} = \frac{i}{4\pi}\left[2n\alpha T_n + (n-k)T_{n-k} + (n+k)T_{n+k} + (k-n)R_{k-n}\right], \tag{57}$$

$$R_{nX} = \frac{i}{4\pi}\left[2n\alpha R_n + (n-k)R_{n-k} + (n+k)R_{n+k} + (k-n)T_{k-n}\right]. \tag{58}$$

The evolution equations (57) and (58) predict the presence of the higher-order harmonics seen in figure 4. Since the only incoming wave is $n = 1$ internal tide, for small X, the only coupling occurs between the $n = 1$ and itself, the $n = 1$ wave and a transmitted $n = k + 1$ wave, and the $n = 1$ wave and a reflected $n = k-1$ wave, as predicted by the linear solution. However, over long topographic length scales, these incited waves will couple to higher order wave numbers and energy will be transferred from the internal tide to other mode numbers by this coupling.

In general, the evolution equations (57) and (58) are a set of coupled linear ordinary differential equations and can be solved by finding the eigenvalues of a system-defining matrix. All the eigenvalues for this matrix are complex, thus the solution is stable. We do not tackle this problem here, but instead focus on a single value for k, $k = 1$.

5.1.2 Analytical solutions for $k = 1$ using a generating function

In the $k = 1$ case, the transmitted and reflected waves are decoupled from each other. Therefore, since there are no reflected waves to begin with, the long length scale evolution of the system only consists of transmitted waves. Furthermore, the evolution equation for the transmitted waves can be solved analytically using a generating function.

We define a generating function, E, as

$$E(X, s) = \sum_{n=1}^{\infty} T_n(X)s^n. \tag{59}$$

If E has an analytical solution, then the coefficients for the transmitted waves are simply

$$T_n(X) = \left.\frac{\partial^{(n)}E}{\partial s^{(n)}}\right|_{s=0}. \tag{60}$$

For $k = 1$, the long length scale evolution of the transmitted waves is given by

$$T_{nX} = \frac{i}{4\pi}\left[2\alpha n T_n + (n-1)T_{n-1} + (n+1)T_{n+1}\right] \tag{61}$$

By multiplying by s^n and summing over n, equation (61) becomes

$$\sum_{n=1}^{\infty} T_{nX} s^n = \frac{i}{4\pi} \sum_{n=1}^{\infty} s^n \left[2nT_n + (n-1)T_{n-1} + (n+1)T_{n+1} \right], \tag{62}$$

and the evolution of the transmitted waves can be expressed in terms of the generating function,

$$E_X = \frac{i}{4\pi} \left(E_s(1 + 2\alpha s + s^2) - T_1 \right). \tag{63}$$

Now to solve for E, we transform E into a function $F(s, X)$,

$$E \to F + \frac{i}{4\pi} \int_0^X T_1(\tilde{X}) d\tilde{X} \tag{64}$$

such that equation (63) can be written as

$$F_X = \frac{i}{4\pi}(1 + 2\alpha s + s^2) F_s. \tag{65}$$

Because

$$\frac{\partial^{(n)} E}{\partial s^{(n)}} = \frac{\partial^{(n)} F}{\partial s^{(n)}}, \tag{66}$$

we only need to solve for F to determine the behavior of the transmitted waves. By a change of variables, the solution to equation (65) is given by

$$F(s, X) = F_0(\zeta - X) \tag{67}$$

where

$$\frac{\partial s}{\partial \zeta} = \frac{i}{4\pi}(1 + 2\alpha s + s^2). \tag{68}$$

The boundary condition at the far left of the domain ($X = 0$) is that the only transmitted wave is the internal tide (i.e. $T_n(0) = 0$ for $n \neq 1$),

$$F(s, 0) = \sum_{n=1}^{\infty} s^n T_n(0) = s. \tag{69}$$

F can be obtained by solving for s in equation (68).

Solution for $h(x) = \frac{1}{2}\cos x$

For the topography $h(x) = \frac{1}{2}\cos x$, $\alpha = 0$ and equation (68) becomes

$$\frac{\partial s}{\partial \zeta} = \frac{i}{4\pi}(1 + s^2). \tag{70}$$

The solution to equation (70) is

$$s = \tan\left(\frac{i\zeta}{4\pi}\right) \text{ or } \zeta = -4\pi i \tan^{-1} s. \tag{71}$$

Substituting the above solution into the left boundary condition (69), we obtain

$$F(s,0) = s = F_0(\zeta) = \tan\left(\frac{i\zeta}{4\pi}\right) \tag{72}$$

and thus,

$$F_0(\zeta - X) = \tan\left(\frac{i(\zeta - X)}{4\pi}\right). \tag{73}$$

We obtain F by substituting for ζ in equation (73),

$$F(s,X) = \frac{s - i\tanh\frac{X}{4\pi}}{1 + is\tanh\frac{X}{4\pi}}. \tag{74}$$

By combining equations (60) and (66), we obtain the transmitted wave coefficients,

$$T_n(X) = (-i)^{(n-1)}\left(1 - \tanh^2\left(\frac{X}{4\pi}\right)\right)\tanh^{(n-1)}\left(\frac{X}{4\pi}\right) \tag{75}$$

For increasing X, the transmitted wave coefficients decay exponentially.

Solution for $h(x) = \frac{1}{2}(\cos x + 1)$

For the topography $h(x) = \frac{1}{2}(\cos x + 1)$, s is given by

$$\frac{\partial s}{\partial \zeta} = \frac{i}{4\pi}(1 + 2s + s^2) = \frac{i}{4\pi}(1+s)^2, \tag{76}$$

whose solution is

$$s = \frac{4\pi i}{\zeta} - 1 \text{ or } \zeta = \frac{4\pi i}{1+s}. \tag{77}$$

Satisfying the boundary condition on F,

$$F_0(\zeta) = \frac{4\pi i}{\zeta} - 1. \tag{78}$$

By substituting $\zeta - X$ for ζ in (78) and for ζ from (77), we obtain F

$$F(s,X) = \left(\frac{1}{1+s} + \frac{iX}{4\pi}\right)^{-1} - 1. \tag{79}$$

The transmitted wave coefficients from equation (60) are

$$T_n(X) = \frac{(-1)^{n-1}\left(\frac{iX}{4\pi}\right)^{n-1}}{\left(1 + \frac{iX}{4\pi}\right)^{n+1}}. \tag{80}$$

As X increases, the transmitted waves decay algebraically, not exponentially, as in the case for the topography $h(x) = \frac{1}{2}\cos x$. The choice of α was initially arbitrary, but the behavior of the solutions seem to diverge significantly. However, in both cases, for large values of X, the waves begin to focus in narrow bands, (see figure 5). The behavior of these solutions for large X is better understood when we move from solutions derived from the streamfunction construction to solutions of the wave equation using the method of characteristics (otherwise known as ray tracing).

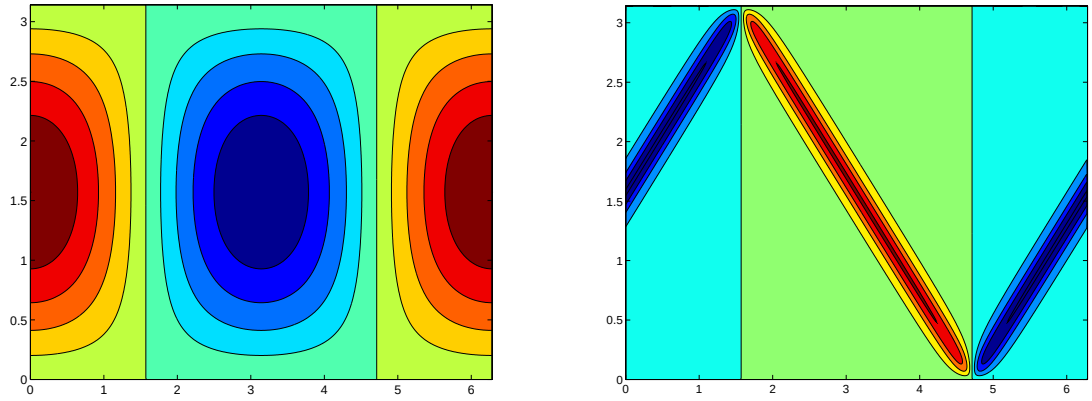

(a) (b)

Figure 5: Contours of the real part of the streamfunction ψ for $h(x) = \frac{1}{2}\cos x$. (a) Streamfunction to the left of the topography. (b) Streamfunction to the right of the topography after 25 topographic wavelengths.

6 Solutions using the method of characteristics

Because the wave equation (7) is hyperbolic, it can also be solved using the method of characteristics. The general solution to the wave equation is

$$\psi = f(x - z) + g(x + z). \tag{81}$$

We define upward characteristics as lines of constant $x - z$ and downward characteristics as lines of constant $x + z$, i.e. characteristics occur along 45° angles (see figure 6). Along these characteristics, we can define Riemann invariants

$$\begin{aligned} R^+ &= \psi_z - \psi_x = u + w, \\ R^- &= \psi_z + \psi_x = u - w, \end{aligned} \tag{82}$$

where $R^+(R^-)$ represents the Riemann invariant on an upward (downward) characteristic.

Characteristics carry a Riemann invariant until they encounter the top or bottom boundary. Along flat boundaries, the boundary condition is such that there is no vertical velocity, $w = 0$. From the definition of the Riemann invariants (82), at a flat boundary (grey region in figure 6), an upward (or downward) characteristic will simply reflect from the boundary, and carry the same Riemann invariant along with it,

$$R^+(x_0, z = \pi) = R^-(x_0, z = \pi). \tag{83}$$

For subcritical topography, when downward characteristics encounter topography (blue region in figure 6) they reflect forwards, but the Riemann invariant is altered. The bottom boundary condition is that there is no normal velocity to the topography,

$$\frac{w}{u} = h_x. \tag{84}$$

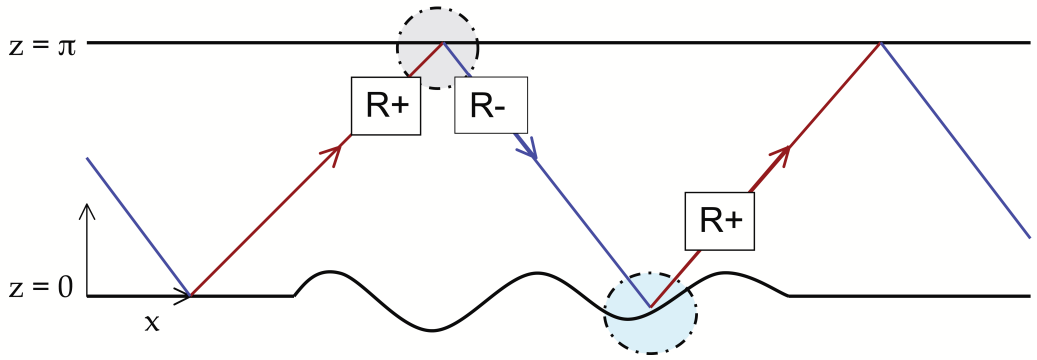

Figure 6: Schematic of tracing characteristics. There is a Riemann invariant $R^+(R^-)$ on upward(downward) characteristics. At a flat boundary, indicated by the grey region, the value of the Riemann invariant is unaffected by reflection ($R^- = R^+$). When a characteristic reflects off topography, e.g. the blue region, the Riemann invariant carried by the characteristic is changed according to equation (85).

The Riemann invariant carried by the reflected upward-going characteristic is then

$$R^+ = R^- \frac{(1 + h_x)}{(1 - h_x)}. \tag{85}$$

In our scaled setup, characteristics that do not encounter topography are 2π-periodic. A characteristic that originates at $(x_0, 0)$ will reflect at the top boundary at $(x_0 + \pi, \pi)$ and return to the bottom boundary at $(x_0 + 2\pi, 0)$. A characteristic that does encounter topography will have its wavelength changed as seen in figure 7. The wavelengths of characteristics that hit the topography where $h > 0$ will shorten, while wavelenths of those characteristics that hit the topography where $h < 0$ will lengthen.

6.1 Solutions for the wave field using Riemann invariants

Characteristics in our reference frame are 2π-periodic, and thus the field determined by the Riemann invariants are also 2π-periodic. If we define a set of Riemann invariants on an interval of length 2π, the wave field can be determined everywhere. The slopes of the topography must remain subcritical for this to be the case; the mapping of characteristics and the definition of the interval over which Riemann invariants must be defined becomes more difficult for slopes that are supercritical (i.e. characteristics can reflect backwards) [12],[13].

Before the topography, the wave field consists only of the internal tide. We define a web of characteristics as a set of upward characteristics uniformly spaced along a flat bottom boundary. The wave field consists of only the internal tide, so the Riemann invariants along the bottom boundary are

$$R^+(x_0) = e^{-ix_0} \tag{86}$$

where x_0 is the origin of the upward characteristic and $x_0 \in [0, 2\pi]$. The value of the Riemann invariants will be altered according to (85) where h_x is evaluated at the point x

such that

$$h(x) = -x + x_0 + 2\pi. \tag{87}$$

The Riemann invariants to the right of the topography are

$$R^+(x_0)_R = \prod_{i=1}^{b} \frac{(1 + h_x(x_i))}{(1 - h_x(x_i))} R^+(x_0)_L, \tag{88}$$

where b is the number of reflections off the bottom (also the number of topographic wavelengths), x_i is the location of the reflection and $x_0 \in [0, 2\pi]$. In the weak topography limit, we can expand equations (85) and (87). The Riemann invariants after the topography are then given by

$$R^+(x_0)_R = (1 + 2\epsilon b h(x_0)) e^{-i(x_0 + 2\epsilon h(x_0))}. \tag{89}$$

Equation (89) recovers the weak topography solution from §3.2.

6.2 Fixed points for model topographies with $k = 1$

We can now determine the behavior of characterstics for our model topographies when $k = 1$. Characteristics that hit the bottom boundary where $h = 0$ will be unchanged in wavelength. Since $\cos x$ is 2π-periodic, these characteristics will reflect at the same relative place on the topography. For those that do not reflect at z=0, the wavelength of the characteristic will change.

Thus, we can characterize the zeros of the topography as either stable or unstable fixed points. Figure 8 shows the behavior of the fixed points for the model topographies, where green indicates a stable fixed point and red indicates and unstable fixed point. For the topography $h(x) = \frac{1}{2}\cos\ x$ in figure 8a, characteristics move towards zeros on positive slopes and move away from zeros on negative slopes. For a stable fixed point located at $(x_s, 0)$, characteristics reflecting at $x_1 > x_s$ will be shortened because $h(x_1) > 0$ and the subsequent bottom reflection will occur at $x_1 > x_2 > x_s$. For multiple reflections, the characteristics will be shortened until the characteristic arrives at $x = x_s$. Characteristics reflecting at $x_1 < x_s$ will be lengthened such that a subsequent reflection will occur at $x_1 < x_2 < x_s$. For an unstable fixed point, x_{us}, characteristics reflecting from $x_1 > x_{us}$ will be lengthened so that $x_1 < x_2$ since $h(x_1) < 0$. Thus, characteristics will move away from the unstable fixed point.

For the topography $h(x) = \frac{1}{2}(\cos\ x + 1)$ in figure 8b, the fixed points are degenerate (two fixed points become a single fixed point). Because the topography is always greater than zero, characteristics not reflecting from a fixed point always shorten. As a result, characteristics will move towards the fixed point on positive slopes and away from the fixed point on negative slopes.

We now interpret the results of §5.1.2 in the context of fixed points of the topography. If we begin to the left of the topography with a web of characteristics that is uniformly distributed along the flat bottom as shown in figure 9a, when these characteristics reflect off topography, their lengths will be altered and the uniform web will become distorted. Subsequent bounces will continue to warp the web such that characteristics will move away from the unstable fixed points and move towards the stable fixed points. After a large number of reflections (equivalent to large X in §5.1.2), the characteristics will be located

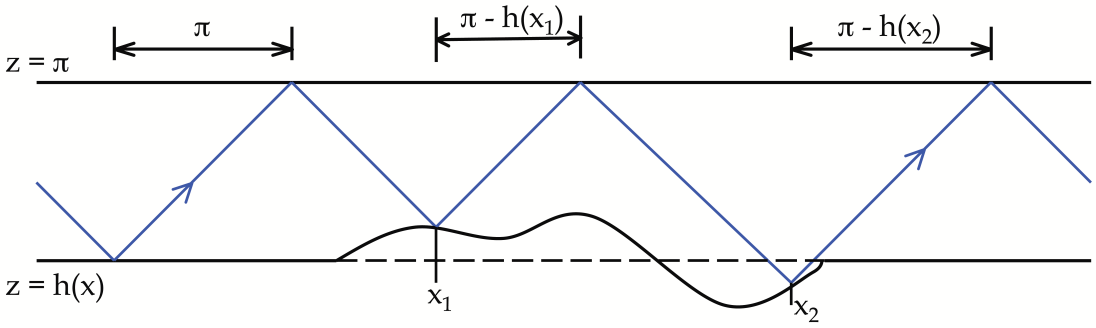

Figure 7: Behavior of characteristics when reflecting off topography. For reflections off the flat bottom ($z = 0$), the wavelength of the characteristics is 2π. When there is positive topography ($h(x) > 0$), the characteristics will shorten by $h(x)$ where x is the reflection point (shown here as x_1). For negative topography, the characteristics will lengthen by $|h(x)|$, (shown as x_2).

in a narrow band around the fixed point as in figure 9b, and the field carried by these characteristics will focus into the narrow band seen in figure 5b.

Recall that the asymptotic solutions for large X differed between the two model topographies; the solution for $h(x) = \frac{1}{2}\cos x$ decayed exponentially while the solution for $h(x) = \frac{1}{2}(\cos x + 1)$ decayed algebraically. The decay behavior is dictated by how rapidly characteristics converge on the fixed points. In the case of the topography $h(x) = \frac{1}{2}\cos x$, characteristics are never more than a distance of π away from a stable fixed point. However, for the topography $h(x) = \frac{1}{2}(\cos x + 1)$, characteristics can be located a distance of up to 2π away from the nearest stable fixed point and as result, characteristics converge on the stable fixed point more slowly.

6.3 Characteristic mapping and solutions for model topographies with $k \neq 1$

Up to this point, we have looked primarily at solutions for the model topographies with $k = 1$. With $k \neq 1$, as seen from the evolution equations, the wave field has reflected waves that propagate leftwards. The Riemann invariants before the topography are not given simply by (86); they also include a (unknown) reflected component that must be solved for as well. Solving for the scattered wave components is not a trivial task. The transmitted waves and reflected waves are coupled; however, for low values of k, the effect of this coupling on the transmitted waves should be minimal. Therefore, the behavior of the transmitted waves should behave similarly to the $k = 1$ case. The characteristics should converge on stable fixed points.

To find the stable fixed points, we can use a 1-D map (figure 10a) to determine the location of the next reflection point given a starting point of x_0. In the map shown in figure 10a, the blue curve plots $x = h(x)$ and the green curve plots $x = x$. The procedure to determine the fixed points are:

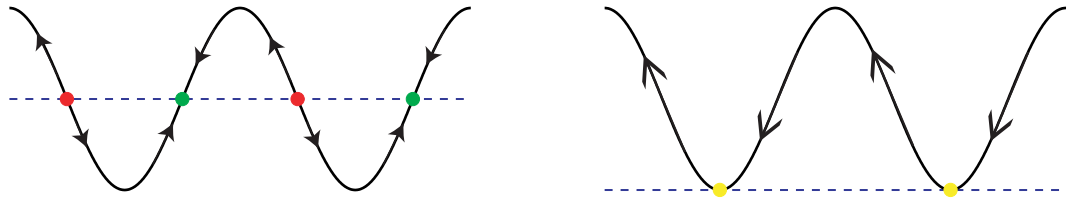

(a) (b)

Figure 8: Behavior of fixed points for (a) $h(x) = \frac{1}{2}\cos x$ and (b) $h(x) = \frac{1}{2}(\cos x + 1)$. The blue dotted line indicates $z = 0$. For the topography in (a), on positive slopes, zeros are stable fixed points (indicated in green). Characteristics will shorten when reflecting to the right of the topography ($h(x) > 0$) and will lengthen when reflecting to the left ($h(x) < 0$). The red points indicate unstable fixed points, and characteristics will move away from them. For the topography in (b), the stable and unstable fixed points collapse onto each other and form a degenerate fixed point (indicated in yellow). Characteristics will focus from the right of the fixed point and diverge to the left.

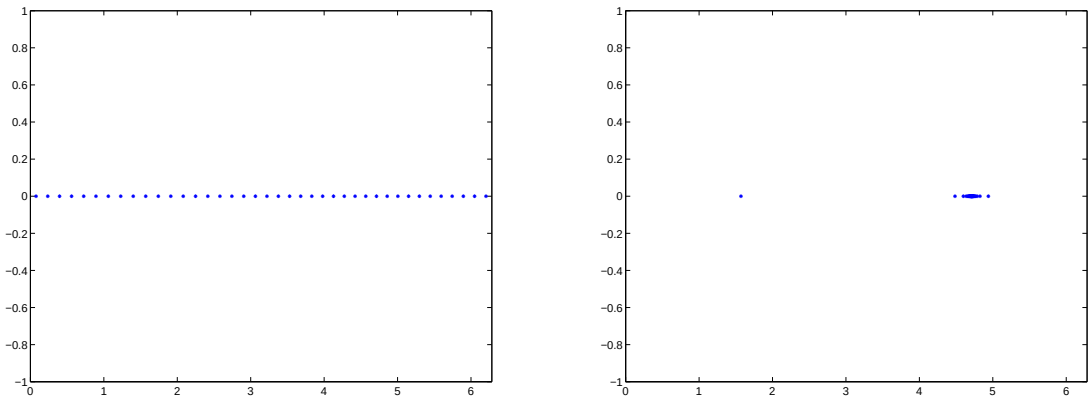

(a) (b)

Figure 9: (a) Origination points for a uniform web of characteristics, defined on the interval $[0, 2\pi]$ to the left of the topography. (b) Web of characteristics after 25 reflections off the topography $h(x) = \frac{1}{2}\cos x$. Characteristics have focused around the stable fixed point.

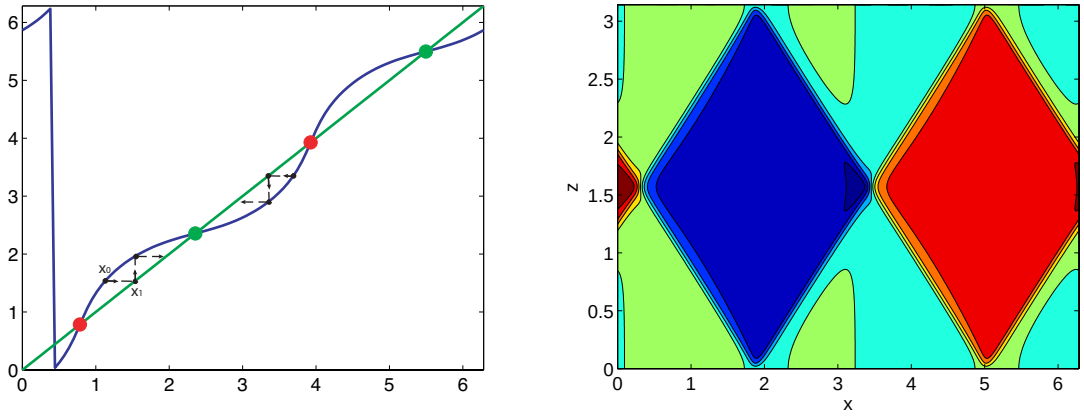

(a) (b)

Figure 10: Behavior of transmitted waves for the topography $h(x) = \frac{1}{2}(\cos 2x + 1)$. (a) 1-D map used to determine fixed points of the topography. (b) Contours of the streamfunction for the transmitted waves on the right side of the topography calculated by the Green's function approach. Waves in (b) are focused around two stable fixed points as predicted by (a).

- A characteristic will begin on the topography on the blue curve at x_0.
- The next reflection point, x_1, can be found by moving along a horizontal line to the green curve.
- The topographic height at x_1 is found by moving along a vertical line to the blue curve.
- A fixed point is a point that maps onto itself. Fixed points occur when the curves $x = h(x)$ and $x = x$ intersect. Characteristics will move towards the stable fixed points and away from the unstable fixed points.

The map for $k = 2$ is shown in figure 10a. The map predicts that the characteristics will converge upon two stable fixed points. Figure 10b shows the numerical solution to the transmitted wave field for $k = 2$ from the Green's function approach. The solution converges onto two stable fixed points.

7 Conclusions

Internal waves propagating in the ocean are likely to encounter long stretches of topography where energy is drained from the low-mode internal tides to and transferred to higher mode numbers. In this work, we primarily looked at model topographies that are unlikely to be found in the ocean. We found that for these special topographies, energy can be transferred rapidly to higher mode number waves. Additionally, characteristics for these topographies

converged onto stable fixed points for topography with multiple reflections. This may be seen as "periodic wave attractors" similar to wave attractors in basins (e.g. [11]).

In the ocean, the bottom topography is not regular and this wave-focusing mechanism is unlikely to be seen. However, we have developed tools that may be utilized for realistic ocean topography. Although computationally expensive, the Green's function approach can provide solutions to the scattering problem over more complex topography. Further work utilizing the method of characteristics may also be valuable to understanding the degradations of the internal tide over random topography.

Acknowledgments

I would like to thank Neil Balmforth and Oliver B$\acute{}$uhler for their countless amounts of patience and assistance throughout the summer. I would also like to thank Bill Young and Joe Keller for their helpful discussions. No GFD summer would be complete without softball, so special thanks to George Veronis for coaching our team. Lastly, thanks to all the fellows and staff for a wonderful summer.

References

[1] P. Baines, *The reflexion of internal/inertial waves from bumpy surfaces*, J. Fluid Mech., 46 (1971), pp. 273–291.

[2] ——, *The generation of internal tides by flat-bump topography*, Deep-Sea Res., 20 (1973), pp. 179–205.

[3] N. J. Balmforth, G. R. Ierley, and W. R. Young, *Tidal Conversion by Subcritical Topography*, J. Phys. Oceanogr., 32 (2002), pp. 2900–2914.

[4] T. H. Bell, Jr., *Statistical features of sea-floor topography*, Deep-Sea Res., 22 (1975), pp. 883–892.

[5] ——, *Topographically Generated Internal Waves in the Open Ocean*, J. Geophys. Res., 80 (1975), pp. 320–327.

[6] P. F. Cummins, J. Y. Cherniawsky, and M. G. G. Foreman, *North Pacific internal tides from the Aleutian Ridge: Altimeter observations and modeling*, J. Mar. Res., 59 (2001), pp. 167–191.

[7] G. D. Egbert and R. D. Ray, *Estimates of M_2 tidal energy dissipation from TOPEX/Poseidon altimeter data*, J. Geophys. Res., 106 (2001), pp. 22,475–22,502.

[8] S. R. Jayne, *The Impact of Abyssal Mixing Parameterizations in an Ocean General Circulation Model*, J. Phys. Oceanogr., 39 (2009), pp. 1756–1775.

[9] S. G. Llewellyn Smith and W. R. Young, *Conversion of the Barotropic Tide*, J. Phys. Oceanogr., 32 (2002), pp. 1554–1566.

[10] ——, *Tidal conversion at a very steep ridge*, J. Fluid Mech., 495 (2003), pp. 175–191.

[11] L. R. M. Maas, D. Benielli, J. Sommeria, and F.-P. A. Lam, *Observation of an internal wave attractor in a confined stable stratified fluid*, Nature, 388 (1997), pp. 557–561.

[12] P. Müller and X. Liu, *Scattering of Internal Waves at Finite Topography in Two Dimensions. Part I: Theory and Case Studies*, J. Phys. Oceanogr., 30 (2000), pp. 532–549.

[13] ——, *Scattering of Internal Waves at Finite Topography in Two Dimensions. Part II: Spectral Calculations and Boundary Mixing*, J. Phys. Oceanogr., 30 (2000), pp. 550–563.

[14] F. Petrelis, S. Llewellyn Smith, and W. R. Young, *Tidal Conversion at a Submarine Ridge*, J. Phys. Oceanogr., 36 (2006), pp. 1053–1071.

[15] L. Rainville and R. Pinkel, *Propagation of Low-Mode Internal Waves through the Ocean*, J. Phys. Oceanogr., 36 (2006), pp. 1220–1236.

[16] H. Sandstrom, *On topographic generation and coupling of internal waves*, Geophys. Astrophys. Fluid Dyn., 7 (1975), pp. 231–270.

[17] L. St. Laurent and C. Garrett, *The Role of Internal Tides in Mixing the Deep Ocean*, J. Phys. Oceanogr., 32 (2002), pp. 2882–2899.